Available online at www.sciencedirect.com
ScienceDirect
Acta Materialia 57 (2009) 5632–5644
Acta MATERIALIA
www.elsevier.com/locate/actamat

# Modeling equiaxed solidification with melt convection and grain sedimentation—II. Model verification

M. Wu *, A. Ludwig

*Simulation and Modeling of Metallurgical Processes, Department of Metallurgy, University of Leoben, A-8700 Leoben, Austria*

Received 2 October 2008; received in revised form 10 July 2009; accepted 28 July 2009
Available online 16 September 2009

**Abstract**

A modified equiaxed solidification model was introduced in Part I. In Part II, a binary Al–Cu alloy casting is simulated using the aforementioned model. Important phenomena accompanying equiaxed solidification considered include: nucleation, globular grain growth, globular-to-dendritic transition, subsequent dendritic growth, recalescence, convection and grain transport. The influence of these events on the formation of the final microstructure (grain size, inter- and extradendritic eutectic) and macrosegregation is also examined. The first verification qualitatively reproduces the features of the previous models. The simulation results are quantitatively compared with the experiments of Nielsen and co-workers [Nielsen Ø, Appolaire B, Combeau H, Mo A. Metall Mater Trans 2001;32A:2049], and a satisfactory agreement is obtained. The new features of the current model and the uncertainty regarding the model assumptions and parameters are studied and discussed. The parameter studies indicate that the grain morphological parameters and the determination of diffusion lengths in different phase regions are the most critical/sensitive factors influencing the quantitative results, and demand further study.


*Keywords:* Simulation; Equiaxed; Al–Cu alloy; Macrosegregation; Eutectic

## 1. Introduction

Since Wang and Beckermann (WB) first reported their equiaxed dendritic solidification model considering melt flow and grain sedimentation [1–3], no significant progress, to the authors' knowledge, has been made. From a practical aspect, the significance of this type of numerical model is vast, as virtually all industrial alloys solidify under normal terrestrial conditions where flow and equiaxed grain sedimentation cannot be avoided. The major difficulty that hinders further development of such a model lies in the complexity of global melt convection and grain transport phenomena at the process scale, which are associated with simultaneous globular and/or dendritic growth kinetics occurring at the microscopic (sub-grid) scale. This has resulted in the authors' proposing a modified model based on the pre existing WB model [1–4] and the Rappaz and Thévoz (RT) model [5–7]. Grain sedimentation and melt convection were addressed using a continuation of the globular equiaxed solidification model, realized by the authors [8,9]. The model was detailed in Part I. In contrast to the previous models, it considers the following features: the globular-to-dendritic transition (GDT); the non-uniform solute distribution in the interdendritic melt region during dendritic solidification; the diffusion-governed solidification of the interdendritic melt; and one hydrodynamic phase for the interdendritic melt and solid dendrites sharing the same velocity.

This paper presents some illustrative modeling results, parameter studies and verifications. The current model is compared with the previous models. Some uncertainties with respect to the model assumptions are also explored. Finally, a comparison of the modeling results with the experimental results/phenomena reported in the literature [10–12] is made.

* Corresponding author. Tel.: +43 3842 4023103; fax: +43 3842 4023102.
*E-mail address:* menghuai.wu@mu-leoben.at (M. Wu).

1359-6454/$36.00 © 2009 Acta Materialia Inc. Published by Elsevier Ltd. All rights reserved.
doi:10.1016/j.actamat.2009.07.067

**Nomenclature**

| | |
|---|---|
| $c_0$ | initial (nominal) concentration of alloy (wt.%) |
| $c_E$ | eutectic concentration (wt.%) |
| $c_e$ | average concentration in equiaxed grains (wt.%) |
| $c_\ell$, $c_d$, $c_s$ | species concentration (wt.%) |
| $c^*$, $c_s^*$ | equilibrium concentration at d–s interface (wt.%) |
| $c_{mix}$ | mix concentration (wt.%) |
| $c_p, c_p^s$ | specific heat (J kg$^{-1}$ K$^{-1}$) |
| $D_\ell$, $D_s$ | diffusion coefficient (m$^2$ s$^{-1}$) |
| $d_e$ | equiaxed grain diameter (m) |
| $f_\ell, f_s, f_d$ | volume fraction of different thermodynamic phases (1) |
| $f_e = f_s + f_d$ | volume fraction of equiaxed phase (1) |
| $f_s^e, f_d^e$ | volume fraction of s- and d-phases within grains (1) |
| $f_e^c$ | equiaxed grain packing limit (1) |
| $f_{Eu}^{total}, f_{Eu}^{extra}, f_{Eu}^{intern}$ | volume fraction of total, extra- and interdendritic eutectic phases (1) |
| $H_w$ | heat transfer coefficient at casting–mold interface (W m$^{-2}$ K$^{-1}$) |
| $k$ | solute partitioning coefficient at the d–s interface (1) |
| $k_\ell$, $k_s$ | thermal conductivity (W m$^{-1}$ K$^{-1}$) |
| $L$ | latent heat (J kg$^{-1}$) |
| $M_{\ell e} (= -M_{e\ell})$ | liquid-equiaxed net mass transfer rate (kg m$^{-3}$ s$^{-1}$) |
| $M_{ds}$ | interdendritic solidification rate (kg m$^{-3}$ s$^{-1}$) |
| $m$ | slope of liquidus in phase diagram (K) |
| $n_{max}$ | maximum equiaxed grain density, or maximum available nucleation sites in heterogeneous nucleation law (m$^{-3}$) |
| $T_0$ | initial temperature (K) |
| $T$ | temperature (K) |
| $T_E$ | eutectic temperature (K) |
| $T_f$ | melting point of pure metal, Al (K) |
| $T_w$ | mold temperature (K) |
| $\Delta T$ | constitutional undercooling (K) |
| $\Delta T_N$ | undercooling for maximum grain production rate (K) |
| $\Delta T_\sigma$ | Gaussian distribution width of nucleation law (K) |
| $t$ | time (s) |
| $\vec{u}, \vec{u}_e$ | velocity vector (m s$^{-1}$) |
| $\Delta \vec{u}$ | relative velocity between melt and grains (m s$^{-1}$) |
| $v_{grob}$ | growth velocity of globular grain (m s$^{-1}$) |
| $v_{env}$ | growth velocity of volume equivalent sphere (m s$^{-1}$) |
| $\beta_T$ | thermal expansion coefficient (K$^{-1}$) |
| $\beta_c$ | solutal expansion coefficient (l) |
| $\beta_s$ | solidification volume shrinkage (l) |
| $\Phi_{Avr}^e$ | Avrami factor for grain impingement (l) |
| $\Phi_{Avr}^s$ | Avrami factor for interdendritic solid impingement (l) |
| $\Phi_{env}$ | shape factor of dendritic grain (l) |
| $\Phi_{sph}$ | sphericity of dendritic grain envelope (l) |
| $\Gamma$ | Gibbs–Thomson coefficient (m K) |
| $\lambda_2$ | secondary dendrite arm space (m) |
| $\mu_\ell$ | viscosity (kg m$^{-1}$ s$^{-1}$) |
| $\rho_\ell$, $\rho_d$, $\rho_s$ | density of thermodynamic phases (kg m$^{-3}$) |
| $\rho_e$ | average density of equiaxed phase (kg m$^{-3}$) |
| $\rho^{ref}, \rho_e^{ref}$ | reference densities of extradendritic melt and equiaxed phase (kg m$^{-3}$) |
| $\Omega$ | supersaturation |

*Subscripts*

| | |
|---|---|
| d | interdendritic melt |
| e | equiaxed grain |
| $\ell$ | extradendritic melt |
| s | interdendritic solid |

## 2. Illustrative benchmark simulation

Solidification of an Al–4.7 wt.% Cu binary alloy was simulated. A two-dimensional square casting ($40 \times 40$ mm$^2$) was meshed into volume elements $2 \times 2$ mm$^2$. The physical and process parameters used are summarized in Table 1. In order to validate the model by comparing the simulation results with the previous modeling and experimental results, the process parameters, the alloy composition and grain morphological parameters were varied. In the current paper, it is assumed that the physical properties remain constant in the alloy composition range, but that the thermodynamic information varies with temperature and concentration in accordance with the phase diagram. Mold filling was ignored. The casting starts to solidify from an initial temperature $T_0$ in a die mold. Both the mold temperature $T_w$ and the heat transfer coefficient at the casting–mold interface $H_w$ are set constant. For the flow calculation, a non-slip boundary condition for both melt and equiaxed phase was applied. The thermal boundary conditions refer to Table 1. Other nucleation and grain morphological parameters are given in the figure captions.

The global solidification sequences are shown in Fig. 1. The relative motion between the grains and the melt due to convection and grain sedimentation is responsible for the formation of weak macrosegregation. Grains start to nucleate and grow from corner and surface regions. As the grains are denser than the melt, they sink and drag the melt with them, inducing two symmetrical vortices (one clockwise on the right and one anticlockwise on the left-hand side). At 0.8 s, the maximum sinking velocity of the grains reaches 1.86 mm s$^{-1}$, while the maximum velocity of the melt is 1.84 mm s$^{-1}$. The relative velocity $\Delta \vec{u}$ is as high as 0.298 mm s$^{-1}$. The melt convection is driven by the thermosolutal buoyancy force and the drag of the sinking grains. The melt is gradually enriched with solute, leaving

Table 1
Parameters used for the process simulations.

| *Thermophysical properties* | *Thermodynamic parameters* |
|---|---|
| $\mu_\ell = 1.3 \times 10^{-2}$ kg m$^{-1}$ s$^{-1}$ | $k = 0.145$ |
| $c_p = 1179$ J kg$^{-1}$ K$^{-1}$ | $m = -344.0$ K |
| $c_p^s = 766$ J kg$^{-1}$ K$^{-1}$ | $T_f = 933.5$ K |
| $D_\ell = 3 \times 10^{-9}$ m$^2$ s$^{-1}$ | $T_E = 821.356$ K |
| $D_s = 8 \times 10^{-13}$ m$^2$ s$^{-1}$ | $c_E = 32.6$ wt.% |
| $L = 3.97 \times 10^5$ J kg$^{-1}$ | $\Gamma = 2.41 \times 10^{-7}$ m K |
| $k_\ell = 77$ W m$^{-1}$ K$^{-1}$ | *Nucleation parameters* |
| $k_s = 53$ W m$^{-1}$ K$^{-1}$ | $n_{max} = 5 \times 10^{11}$ m$^{-3}$ (varied for parameter study) |
| $\beta_T = 10^{-4}$ K$^{-1}$ | $\Delta T_N = 5$ K |
| $\beta_c = 9.2 \times 10^{-3}$ wt.%$^{-1}$ | $\Delta T_\sigma = 2$ K |
| $\rho_\ell(\rho_d, \rho_e) = 2606$ kg m$^{-3}$ | *Process conditions* |
| $\rho^{ref}(\rho_e^{ref}) = 2606$ kg m$^{-3}$ | $c_0 = 4.7$ wt.% (varied for parameter study) |
| $\rho_s = 2743$ kg m$^{-3}$ | $T_0 = 922$ K (varied for parameter study) |
| $\beta_s = (\rho_s - \rho)/\rho_e^{ref} = 0.0526$ | $H_w = 500$ W m$^{-2}$ K$^{-1}$ |
| | $T_w = 290$ K |

solute-depleted grains. The grains which sink from the top surface region, especially near the corner, cause the formation of a positive segregation layer. This occurs because the denser solute-poor grains move away from the corner, leaving a solute-enriched melt behind. It is clear that the solute-depleted grains move to the neighboring region, just a few millimeters beneath the top surface area, to form a negative segregation layer. This same mechanism operates in the lower region, where a negative segregation layer forms at the bottom surface, with a weak positive segregation layer situated a few millimeters above. In the lower corner, the negative segregation is slightly greater, because more grains sink and settle along the wall.

As solidification proceeds, at 10 s, the equiaxed grains occur throughout the entire cast section. The volume fraction of grains $f_e$ in the lower corners reaches a maximal value of 0.86, considerably greater than the packing limit (0.637), thereby preventing movement. Conversely, $f_e$ in the casting center is only 0.01. The grains in this or other regions, where $f_e$ is lower than the packing limit, continue to sink downwards. The flow pattern of the melt is completely different from the flow pattern at the initial stage. In the upper section, in the lower corner and near the packing regions, however, the melt flows upwards. Two symmetrical vortices (one clockwise on the right-hand side and one anticlockwise on the left-hand side) still remain, but they are confined to the casting center region. The relative velocity between the two phases $\Delta\vec{u}$, which reaches a maximum value of 1.07 mm s$^{-1}$, always points downwards. The upper positive segregation (zone) becomes increasingly strong and wide. For the same reason, the solute-depleted grains continue to leave the upper center region, and the solute-enriched melt feeds this region. The negative segregation zone just beneath this positive segregation zone moves with the same velocity as the sinking grains. In the lower region, the negative segregation zone also becomes stronger and wider. The lower corner of the negative segregation zone gradually stretches towards the casting center. The positive segregation band in front of the lower negative segregation zone becomes increasingly pronounced, and gradually shifts upwards.

At 20 s, there is only a small area close to (slightly above) the geometrical center, where grains can still move. The relative motion between the sinking grains and the melt is very clear. As the grains sink, the melt flows in the reverse direction. This means that the solute-enriched melt tends to separate from the solute-depleted grains. This type of relative motion speeds up segregation formation. A relatively large and strong segregated zone forms in the upper section of the casting. The negative segregation in the upper part continues to move downwards with the sinking grains. The negative segregation zone from the lower corner continues to extend towards the casting center, finally joining with the upper negative segregation zone, to form a Λ-shape (Fig. 1). The positive segregation zone, which formed in front of the lower bottom negative segregation zone at an early stage, disappears up to this moment, because this positive segregation zone is cancelled out by the approaching negative segregation zone from the upper part (as a consequence of the grain sedimentation).

The casting takes 40.3 s to solidify completely. The final solidification results are summarized in Fig. 2. A prediction of the grain size distribution $d_e$ showed a general tendency for fine grains to occur in the outer corner and surface region, and relative coarse grains in the inner region. However, the distribution between the lower and the upper parts is uneven, with the coarsest grains distributed a few centimeters above the geometrical center. In order to investigate the influence of flow and sedimentation on the microstructure, a second simulation with the same process parameters but without flow and sedimentation was performed. The simulation results with and without considering flow and sedimentation are summarized in Table 2. It was demonstrated that the effect of convection and sedimentation causes a more uneven distribution of the structure ($d_e$, $f_{Eu}^{extra}$, $f_{Eu}^{intern}$ and $f_{Eu}^{total}$). The structural inhomogeneity between the outer surface and the inner surface regions was due to the different cooling rates, but the uneven distribution between the upper and lower parts was caused by the convection and grain sedimentation (Fig. 2).

The final macrosegregation pattern shown in Fig. 2 was the direct outcome of the convection and grain sedimentation. The positive segregation zone with maximum $c_{mix}$ (5.0 wt.%) was located in the upper region. The negative segregation zone with minimum $c_{mix}$ (4.53 wt.%) was located in the middle and lower casting sections. The top casting surface had a positive segregation of $c_{mix} = 4.8$ wt.%, the bottom surface had a negative segregation of $c_{mix} = 4.62$ wt.%, and the regions near the side walls had an almost neutral concentration with $c_{mix} = 4.7$ wt.%.

## 3. Phase evolution and microstructure formation

The simulation of the benchmark without flow and grain sedimentation was further analyzed. The phase evo-

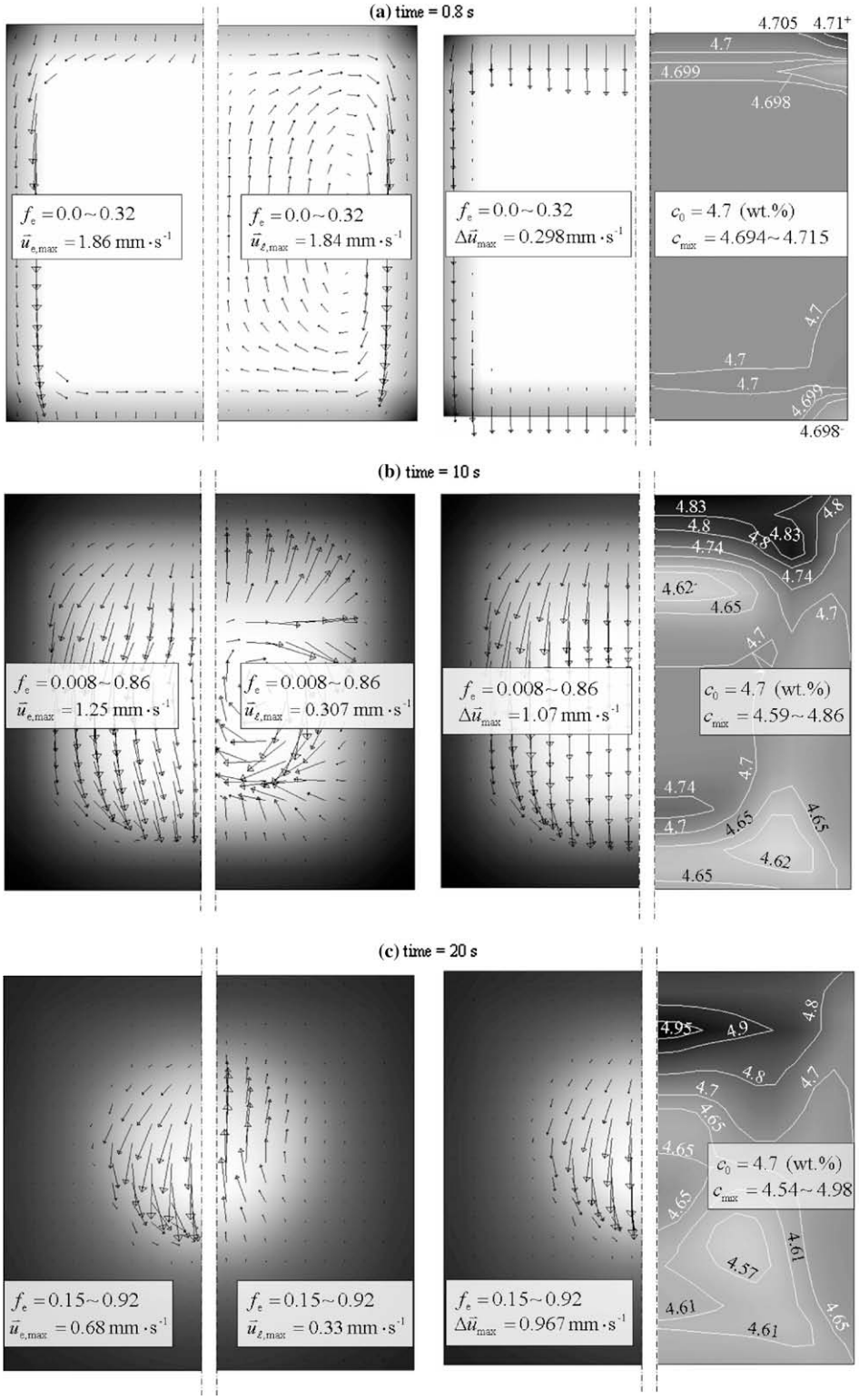


Fig. 1. Solidification sequence of an Al–4.7 wt.% Cu square casting. The volume fraction of the equiaxed grains $f_e$ is shown using gray scales, with dark for the highest and light for the lowest value. The vectors of the velocity fields $\vec{u}_e$ and $\vec{u}_\ell$ are overlaid with $f_e$. The relative velocity is also shown ($\Delta\vec{u} = \vec{u}_e - \vec{u}_\ell$). The mixture concentration $c_{mix}$ is shown using a gray scale and overlaid with isolines. The nucleation parameters used are $n_{max} = 5 \times 10^{11}\ m^{-3}$, $\Delta T_\sigma = 2$ K, $\Delta T_N = 5$ K; grain morphological parameters are $\Phi_{env} = 0.6827$, $\Phi_{sph} = 0.283$ and $\lambda_2 = 10$ μm.

lution at a representative point in the casting corner is shown in Fig. 3. The evolution of the microstructure has been divided into four stages.

Nucleation events start at 0.5 s when the local temperature drops below the liquidus (917.3 K). The grains start to grow with globular morphology (stage I). According to the

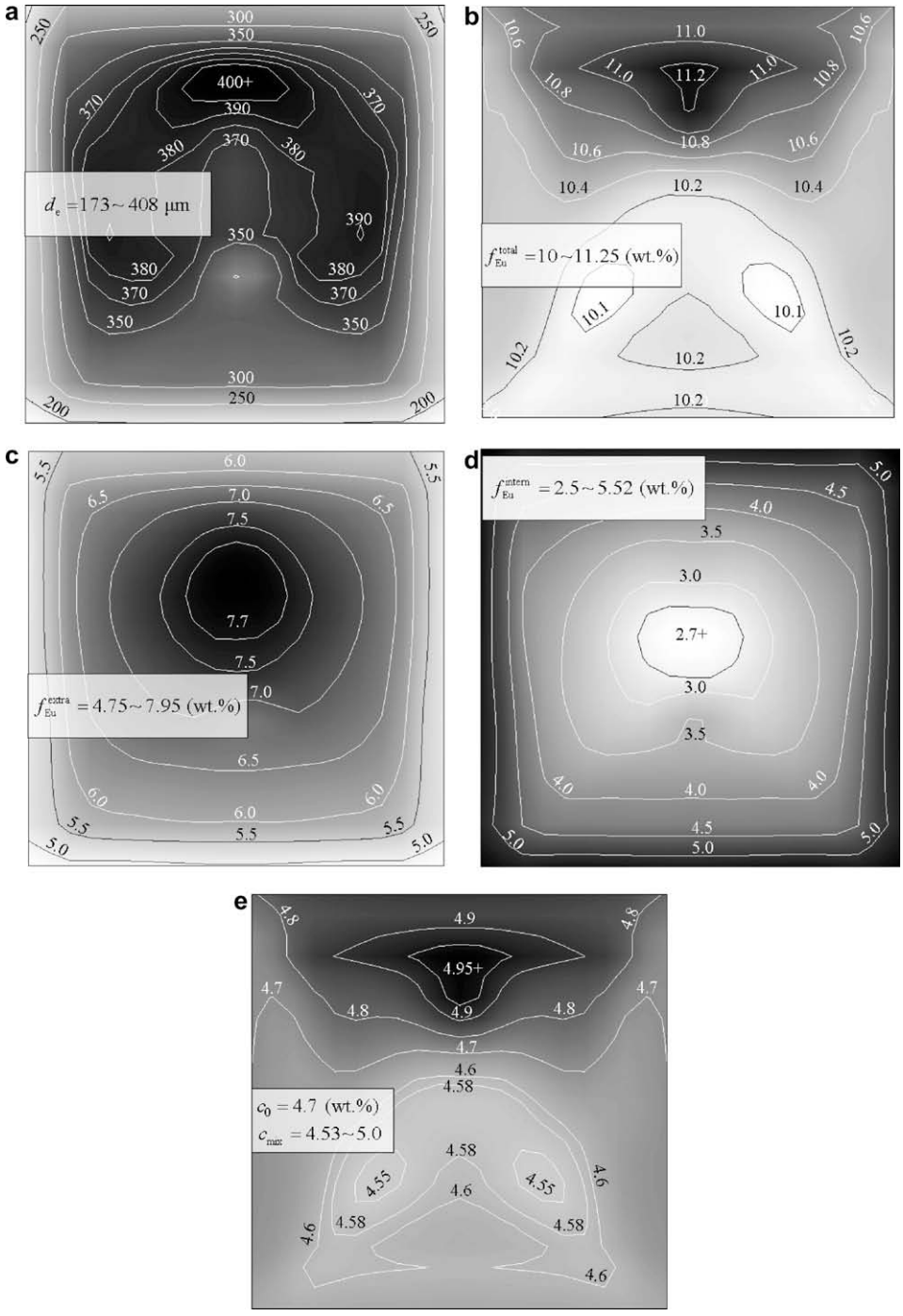


Fig. 2. Final microstructure and macrosegregation of the square casting (Al–4.7 wt.% Cu). All the quantities are shown using gray scale (dark for the highest and light for the lowest value) and isolines. Nucleation parameters are $n_{max} = 5 \times 10^{11}$ m$^{-3}$, $\Delta T_\sigma = 2$ K and $\Delta T_N = 5$ K; and grain morphological parameters are: $\Phi_{env} = 0.6827$, $\Phi_{sph} = 0.283$ and $\lambda_2 = 10$ μm.

model assumption, GDT occurs when the calculated growth velocity of the volume equivalent sphere $v_{env}$ overtakes the globular grain growth velocity $v_{glob}$. Here, $v_{env}$ is calculated according to Lipton–Glicksman–Kurz (LGK) dendrite tip growth kinetics [13,14]. As shown in Fig. 3a, at the initial stage, $v_{glob} > v_{env}$, so the grains grow with globular morphology. There is no interdendritic melt, i.e., $f_s^e \equiv 1$. The mass transfer rate from extradendritic melt to the equiaxed grain, $M_{\ell e}$, is identical to the solidification rate $M_{ds}$. Both quantities, however, are quite small (in the order of $10^{-3}$–$10^{+1}$ kg m$^{-3}$ s$^{-1}$) at the initial stage. Solute partitioning occurs directly at the liquid–solid interface between the grain and extradendritic melt. The solute in the extradendritic melt $c_\ell$ is slightly enriched, but this enrichment is small and undetectable because the magnitude of the local $f_e$ is still in the order of $10^{-5}$. At the point of GDT (0.11 s), $c_\ell$ is only 4.700193 wt.% (the nominal composition is 4.7 wt.%), and $d_e$ is ~6 μm. Owing to the

Table 2
Influence of convection flow and grain sedimentation on the microstructure and macrosegregation of an Al–4.7 wt.% Cu alloy.

| Simulation cases | $d_e$ (m) | | $f_{Eu}^{extra}$ (wt.%) | | $f_{Eu}^{intern}$ (wt.%) | | $f_{Eu}^{total}$ (wt.%) | | $c_{mix}$ (wt.%) | |
|---|---|---|---|---|---|---|---|---|---|---|
| | From | To | From | To | From | To | From | To | From | To |
| With flow and sedimentation | 173 | 408 | 4.75 | 7.95 | 2.5 | 5.52 | 10 | 11.25 | 4.53 | 5.0 |
| Without flow and sedimentation | 176 | 393 | 4.86 | 7.7 | 2.8 | 5.47 | 10.3 | 10.5 | No macrosegregation | |

small solidification rate at this initial stage, the latent heat released is so small that the temperature continues to drop.

Stage II, also referred to as "free" dendritic growth, starts with the GDT at 0.11 s, and ends at 0.15 s when recalescence begins, i.e., the moment when the cooling curve reaches its lowest extreme, which coincides with $c_\ell^*$ and $v_{env}$ peaks. During this "free" dendritic growth period, the dendrite tip velocity increases dramatically, and the equiaxed grains grow rapidly from 6 to ~36 μm in a very short period (0.04 s). The skeleton of the dendrites becomes more stretched correspondingly, and $f_s^e$ decreases from 1 to 0.2. $M_{\ell e}$ is much larger than $M_{ds}$. The latent heat released due to $M_{ds}$ is still not high enough to compensate for the heat subtracted by the global heat extraction rate, and the temperature continues to drop until the end of stage II. A particular feature of stage II is the non-uniform solute distribution in the interdendritic melt. The volume-averaged interdendritic melt concentration $c_d$ is equal to neither the thermodynamic equilibrium concentration $c_\ell^*$ which applies at the liquid–solid interface, nor the averaged concentration at the grain envelope $\bar{c}_{env}$ (Fig. 3, Part I). $\bar{c}_{env}$ is calculated according to WB [4], i.e., $\bar{c}_{env} = (l_d c_\ell + l_\ell c_d)/(l_d + l_\ell)$. Immediately after the GDT, a large amount of melt with the average concentration $\bar{c}_{env}$, which is initially very close to the extradendritic melt concentration $c_\ell$, is enveloped in the grain, causing the average interdendritic melt concentration $c_d$ to drop dramatically from $c_\ell^*$. Therefore, a large difference between $c_\ell^*$ and $c_d$ is immediately established. This immediately established concentration difference $(c_\ell^* - c_d)$ is the driving force for the interdendritic melt solidification $M_{ds}$). The interdendritic melt solidification, in turn, enhances the enrichment of the interdendritic melt concentration $c_d$ due to the solute partitioning ($k < 1$) at the solid–liquid interface. Obviously, competition arises between the growth of the grain envelope and the solidification of the interdendritic melt. The growth of the grain envelope tries to enclose more extradendritic melt with average concentration $\bar{c}_{env}$ into the grain envelope, causing $c_d$ to decrease. Conversely, the larger $M_{ds}$ due to the increasing $c_\ell^* - c_d$ causes $c_d$ to recover to the level of $c_\ell^*$. At the same time, the large $M_{ds}$ leads to the release of large amounts of latent heat, and as a consequence the cooling rate slows down. As soon as the latent heat released by the solidification of the interdendritic melt is balanced by the external heat extraction rate, the local temperature ceases to decrease, and recalescence occurs, which signals the end of stage II.

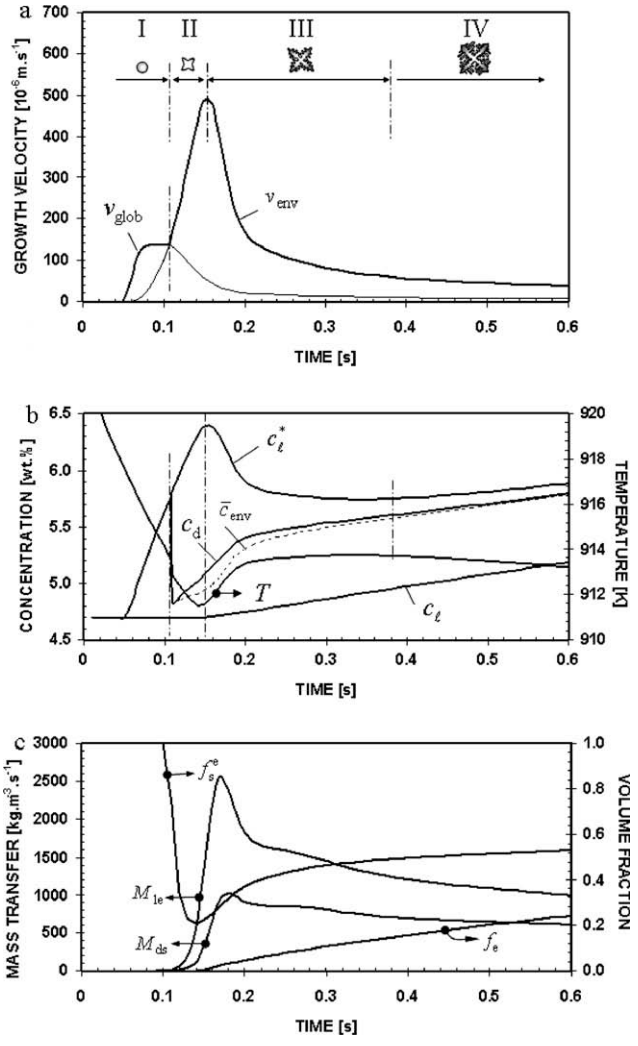


Fig. 3. Calculated phase evolution (Al–4.7 wt.% Cu) located at the corner of the casting: (a) grain growth velocity; (b) concentrations in different phase regions together with cooling curve; and (c) mass transfer rates and volume fractions of phases.

Stage III begins and ends with the recalescence, and it is referred to hereafter as dendritic growth with recalescence. The increasing $M_{ds}$ induces the release of a large amount of latent heat. When the latent heat released overcomes the external heat extraction rate, recalescence occurs. The growth velocity of the grain envelope decreases gradually with the recalescence, as the driving force for the growth of the dendrite tips, $\Omega = (c_\ell^* - c_\ell)/(c_\ell^* - c_s^*)$, is reduced with the rise in temperature. During this period, $c_\ell^*$ and $c_d$ become increasingly close, and the interdendritic melt

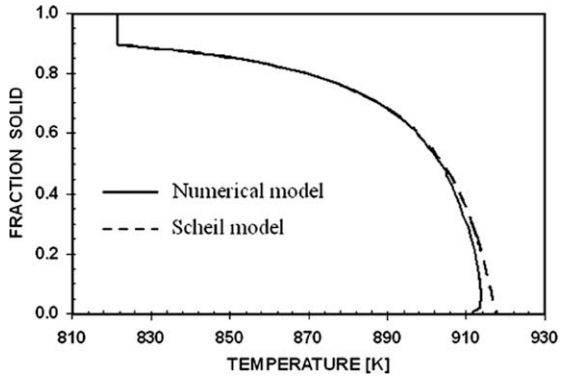


Fig. 4. Comparison of the numerically calculated $f_s$–$T$ curve with that of the Scheil model.

solidification rate $M_{ds}$ becomes gradually smaller until the latent heat released by the interdendritic melt solidification is balanced with the global heat extraction rate. One significant difference between stages II and III is that the envelope growth velocity $v_{env}$ increases during stage II, while decreasing during stage III. The estimated $\bar{c}_{env}$ is lower than $c_d$, with the difference between them relatively large during stage II. This difference decreases during stage III. At the end of stage III, $\bar{c}_{env}$ approaches $c_d$.

Stage IV is referred to as either "confined" dendritic growth or "coarsening/dendrite arm thickening" [5]. The grain envelope cannot significantly grow further owing to two mechanisms of impingement. One is the enrichment of $c_\ell$ with its corresponding reduction/disappearance of supersaturation $\Omega$. Another mechanism is mechanical impingement, which is accounted for by an Avrami factor $\Phi^e_{Avr}$ in this current model. However, the interdendritic melt solidification will continue. During this stage, $c_d$ approaches $c^*_\ell$. At the very end of solidification (not seen in Fig. 3), the difference between $c_d$ and $c_\ell$ becomes increasingly small, until the enrichment of $c_\ell$ is so high that all those concentrations ($c_\ell$, $c_d$ and $c^*_\ell$) approach the eutectic concentration $c_E$. This result indicates that complete mixing ($c_d \approx c^*_\ell$) in the interdendritic melt will happen relatively soon, while complete mixing with the extradendritic region will take place only at the latest stage of solidification.

A $f_s$–$T$ curve is plotted in Fig. 4, which is compared with the Scheil model. It should be noted that the two curves are, not exactly but almost, superimposed on each other at the end of solidification. A relatively large deviation close to the liquidus temperature, corresponding to the "free" dendrite growth and recalescence stages, was predicted. It implies that the Scheil-assumption of complete mixing of the inter- and extradendritic melt ($c_d$, $c_\ell$ and $c^*_\ell$) can be valid during the late stages of solidification but not at the initial stage. However, the initial solidification stage is actually the most critical moment for the evolution of the dendritic structure.

The phase evolution processes under differing cooling conditions were also analyzed in Fig. 5. The general phase evolution procedures are quite similar, regardless of the cooling conditions. They start to grow with globular morphology, then the GDT occurs, and finally they remain dendritic until the eutectic phases form in the interdendritic and extradendritic regions. However, quantitative differences are observed. At the lower corner, the cooling rate is very high. The globular growth starts immediately as the cooling starts, and then the GDT occurs at ~0.11 s. At the casting center, the cooling rate is quite low. The globular solidification starts at ~6 s, and the GDT occurs at 8.6 s. As a consequence (Table 2), more interdendritic eutectic phase is predicted in the corners ($f^{intern}_{Eu} = 5.47$ wt.%) than in the center of the casting ($f^{intern}_{Eu} = 2.8$ wt.%), and less extradendritic eutectic in the corners ($f^{extra}_{Eu} = 4.86$ wt.%) than in the casting center ($f^{extra}_{Eu} = 7.7$ wt.%).

The influence of the nucleation parameters on the intensity of the recalescence, as studied previously [4,5], was also examined (Fig. 6). The cooling curves at two different locations were plotted and compared. The recalescence phenomenon was found to be more pronounced at lower nucleation rates (coarse-grained). It was also found that the larger the cooling rate (i.e., at the corner of the casting), the more pronounced the recalescence phenomenon. No clear recalescence was measured at the casting center. This prediction agrees with the previous work [4,5].

## 4. Comparison with experimental results

Al–Cu binary alloy samples with different compositions were cast and analyzed by Nielsen et al. [10]; the results are shown in Fig. 7 (∗ points). The average heat extraction rate from the experimental samples was ~4.7–5.6 × $10^3$ J

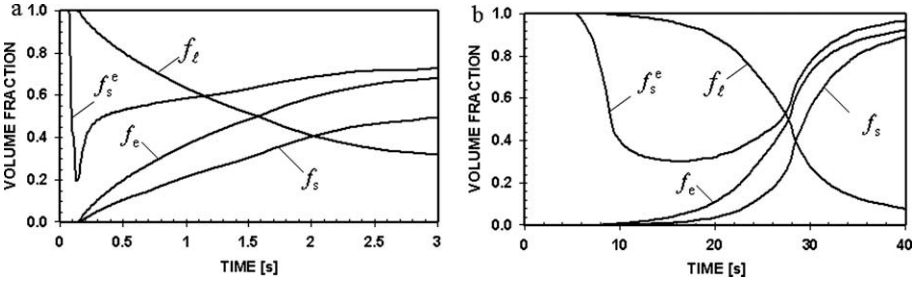


Fig. 5. Influence of cooling conditions on the phase evolution in the square casting (Al–4.7 wt.% Cu) (a) at the corner and (b) in the casting center. Nucleation parameters are $n_{max} = 5 \times 10^{11}$ m$^{-3}$, $\Delta T_\sigma = 2$ K and $\Delta T_N = 5$ K; grain shape factors are $\Phi_{env} = 0.6827$, $\Phi_{sph} = 0.283$ and $\lambda_2 = 10$ μm. No flow is considered.

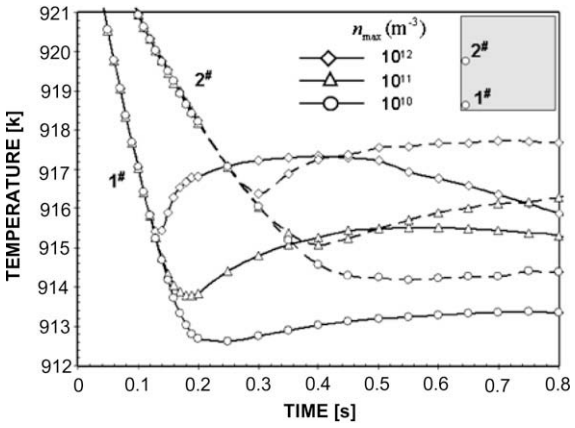


Fig. 6. Influence of cooling conditions and nucleation rates on the recalescence (Al–4.7 wt.% Cu).

$kg^{-1}\,s^{-2}$, corresponding to a solidification time of ~48 s. The final grain number density $n$ was measured as 0.18–$2.3 \times 10^{11}\ m^{-3}$, and the secondary dendrite arm spacing $\lambda_2$ was ~26–42 μm. In the current numerical model, the same rectangular casting geometry as described in Section 2 was considered, but the alloy composition was varied from 4 to 15 wt.% Cu. With a constant heat transfer coefficient, 500 $W\,m^{-2}\,K^{-1}$, the casting took ~41 s to solidify. With the nucleation parameters as given in the caption of Fig. 7, a final grain density between $0.3 \times 10^{11}\ m^{-3}$ in the center and $3.7 \times 10^{11}\ m^{-3}$ at the corner was predicted. The processing conditions were comparable with those of the experiments.

In order to perform the calculations, morphological parameters ($\Phi_{sph}$, $\Phi_{env}$ and $\lambda_2$) were required. Here, parameter studies were performed and were based on the assumptions made for the above morphological parameters. For example, the first group of modeling results were obtained assuming an ideal spherical envelope enclosing outer primary dendrite tips [5,6], i.e., both $\Phi_{sph}$ and $\Phi_{env}$ were 1. The secondary dendrite arm spacing $\lambda_2$ was 10 μm. The calculated results are represented in Fig. 7 by symbol ○. It was found that the predicted total eutectic phase was close to the experimental result. The lower the alloy composition, the better the agreement between the modeling and experimental results. The relatively large discrepancy using a high-alloy composition was due to the neglect of the latent heat from the eutectic reaction and the neglect of back diffusion into the solid dendrites. The numerical prediction of the extra- and interdendritic eutectic was significantly different from the experimental results.

A second group of calculations were made assuming an octahedral grain envelope [10], $\Phi_{env} = 0.683$, $\Phi_{sph} = 0.85$. The results are represented by symbol ● in Fig. 7. The predicted volume fractions of extra- and interdendritic eutectic were slightly closer to the experimental results when compared with the case of the ideal spherical envelope enclosing outer primary dendrite tips, but the discrepancy from the experiments was still very large.

As described in Part I, for the dendritic grain which was described with the "natural" contour enclosing the primary and secondary dendrite tips, both $\Phi_{env}$ and $\Phi_{sph}$ can be much smaller than 1. Therefore, further calculations with smaller $\Phi_{env}$ and $\Phi_{sph}$ were made. For example, the modeling results when assuming $\Phi_{env} = 0.577$ and $\Phi_{sph} = 0.283$ are represented in Fig. 7 by the symbol ♦. Not only the total eutectic, but also the predicted inter- and extradendritic eutectic phases were close to the experimental results. One could anticipate that further calculations by adjusting $\Phi_{env}$ and $\Phi_{sph}$ would lead to a modeling result that would fit the experimental data.

In the above simulations, a constant secondary dendrite arm space ($\lambda_2 = 10$ μm) was used, which was different from the experimentally measured value (26–42 μm). According to the current model, $\lambda_2$ is an important quantity governing

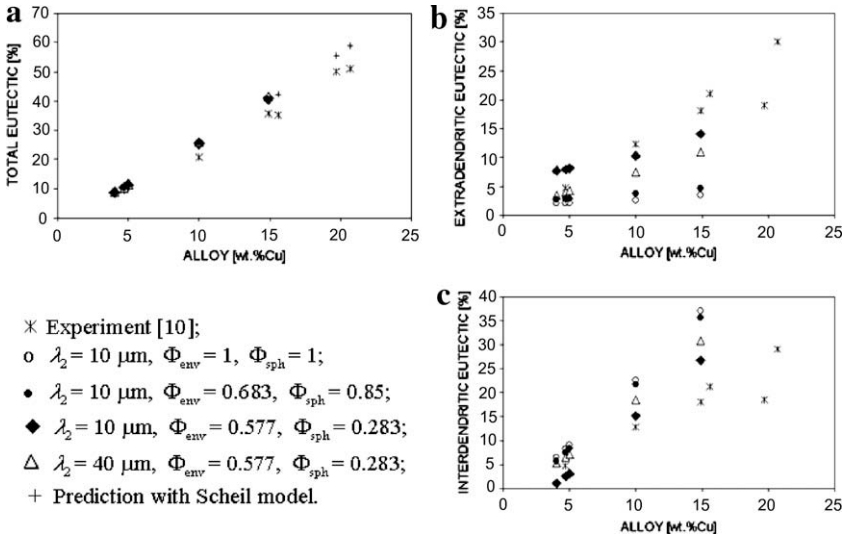


Fig. 7. Comparison of the modeling and experimental results [10]: (a) volume fraction of total eutectic as a function of alloy composition; (b) extradendritic eutectic; and (c) interdendritic eutectic. Nucleation parameters: $n_{max} = 5 \times 10^{11}\ m^{-3}$, $\Delta T_\sigma = 2$ K and $\Delta T_N = 5$ K.

the solidification of interdendritic melt (Part I). Therefore, an additional group of simulations with different $\lambda_2$ (40 m) were performed, and the results are identified by the symbol △ in Fig. 7. No significant influence on the total eutectic was found on increasing $\lambda_2$ by a factor of 4. However, more interdendritic eutectic phase was obtained with a larger $\lambda_2$. The larger $\lambda_2$ slows down the solidification rate of the interdendritic melt.

Although different morphological grain parameters are used, all the modeling results regarding the total eutectic $f_{\mathrm{Eu}}^{\mathrm{total}}$ formed during solidification are similar (Fig. 7a). $f_{\mathrm{Eu}}^{\mathrm{total}}$ seems to be independent of the morphological parameters. One fact, which is evident in Fig. 4, is that the current model predicts that the $f_s$–$T$ curve almost superimposes the Scheil curve at the end of solidification. Therefore, $f_{\mathrm{Eu}}^{\mathrm{total}}$ was calculated based on the Scheil model, and plotted with the symbol + on the same curve (Fig. 7a). It is not a surprise that the modeling results of $f_{\mathrm{Eu}}^{\mathrm{total}}$ closely agree with those of the Scheil model.

The above parameter studies imply that: (1) the envelope of the real dendritic grain (Al–Cu) would be quite different from the octahedral and spherical envelopes; and (2) the morphological parameters are critical for quantitative prediction of the inter- and extradendritic eutectic phase, but that the total amount of the eutectic phase formed is almost independent of the aforementioned morphological parameters assumed.

## 5. Dendritic solidification vs globular solidification

The same Al–4.7 wt.% Cu casting was simulated with a "pure" globular equiaxed solidification model developed by the authors [8,9], in which no dendritic growth was considered. The simulation results were compared with those of the current dendritic solidification model (Section 3). The solidification time in the globular solidification model was 40.8 s, comparable with 40.3 s for the case of dendritic solidification. The solidification time was governed mainly by the global heat transfer and was less sensitive to the grain growth morphology.

The final microstructure and macrosegregation are shown in Fig. 8. The average grain size distribution $d_e$ was predicted to be in the range 141–231 μm, which is much smaller than that of dendritic grains (173–408 μm). The distribution pattern of $d_e$ was also different from the case of dendritic solidification. The large grains did not accumulate in the casting center, but in the top surface region and in regions some distance from the side and bottom walls. In the globular solidification, there was no interdendritic eutectic, and the amount of total eutectic $f_{\mathrm{Eu}}^{\mathrm{total}}$ was identical to the amount of $f_{\mathrm{Eu}}^{\mathrm{extra}}$. A gradient distribution of $f_{\mathrm{Eu}}^{\mathrm{extra}}$ from the bottom (9.115 wt.%) to the top surface (17.35 wt.%) was predicted. The distribution pattern of $c_{\mathrm{mix}}$ was similar to the distribution pattern of $f_{\mathrm{Eu}}^{\mathrm{extra}}$. The largest positive segregation zone was located on the top surface (6.53 wt.%), while the largest negative segregated zone was located at the bottom (4.17 wt.%). The segregation was much stronger than in the case of dendritic solidification.

Fig. 9 shows the globular equiaxed solidification sequence in more detail. It helps to explain the macrosegregation formation in this case. The formation mechanisms for the macrosegregation by grain sedimentation are actually the same as those of the dendritic solidification. However, the solute exchange at the grain–melt interface and the velocity fields are quantitatively different. Therefore, the strength and distribution pattern of $c_{\mathrm{mix}}$ are different.

At the initial stage, the evolution of the volume fraction of the globular grains $f_e$ is slower. At 0.8 s, the maximum volume fraction of the grains $f_e$ is only 0.12. On the top surface, a positive segregation layer forms because the solute-depleted grains are transported away from this layer, leaving solute-enriched melt behind. Just beneath this positive segregation layer, a negative zone (layer) forms where the grains accumulate. At the lower bottom, a negative segregation layer starts to build up. Just above the bottom negative segregation layer, an area of positive segregation forms. The macrosegregation predicted by the "pure" globular solidification model at the initial stage is not as strong as the macrosegregation predicted by the dendritic solidifi-

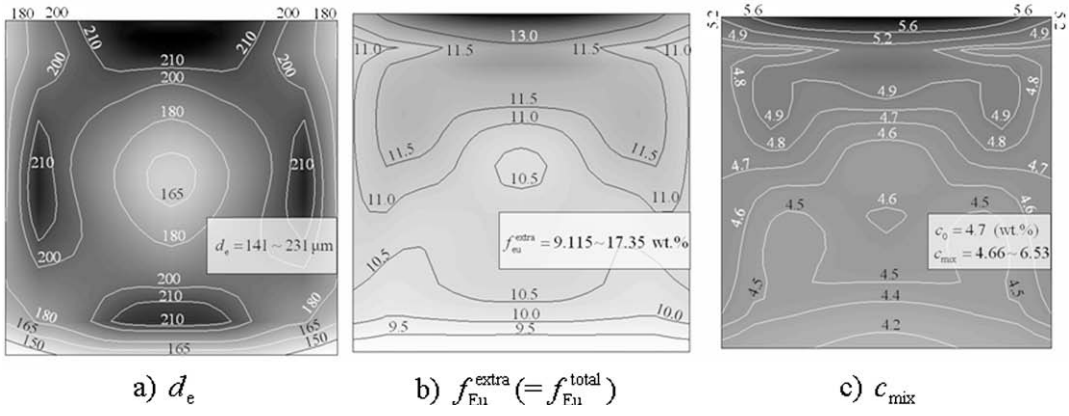


Fig. 8. Final microstructure and macrosegregation of the square casting (Al–4.7 wt.% Cu) predicted with the "pure" globular solidification model [8,9]. All the quantities are shown in both gray scale and isolines. Nucleation parameters are $n_{\max} = 5 \times 10^{11}\ \mathrm{m}^{-3}$, $\Delta T_\sigma = 2$ K and $\Delta T_N = 5$ K.

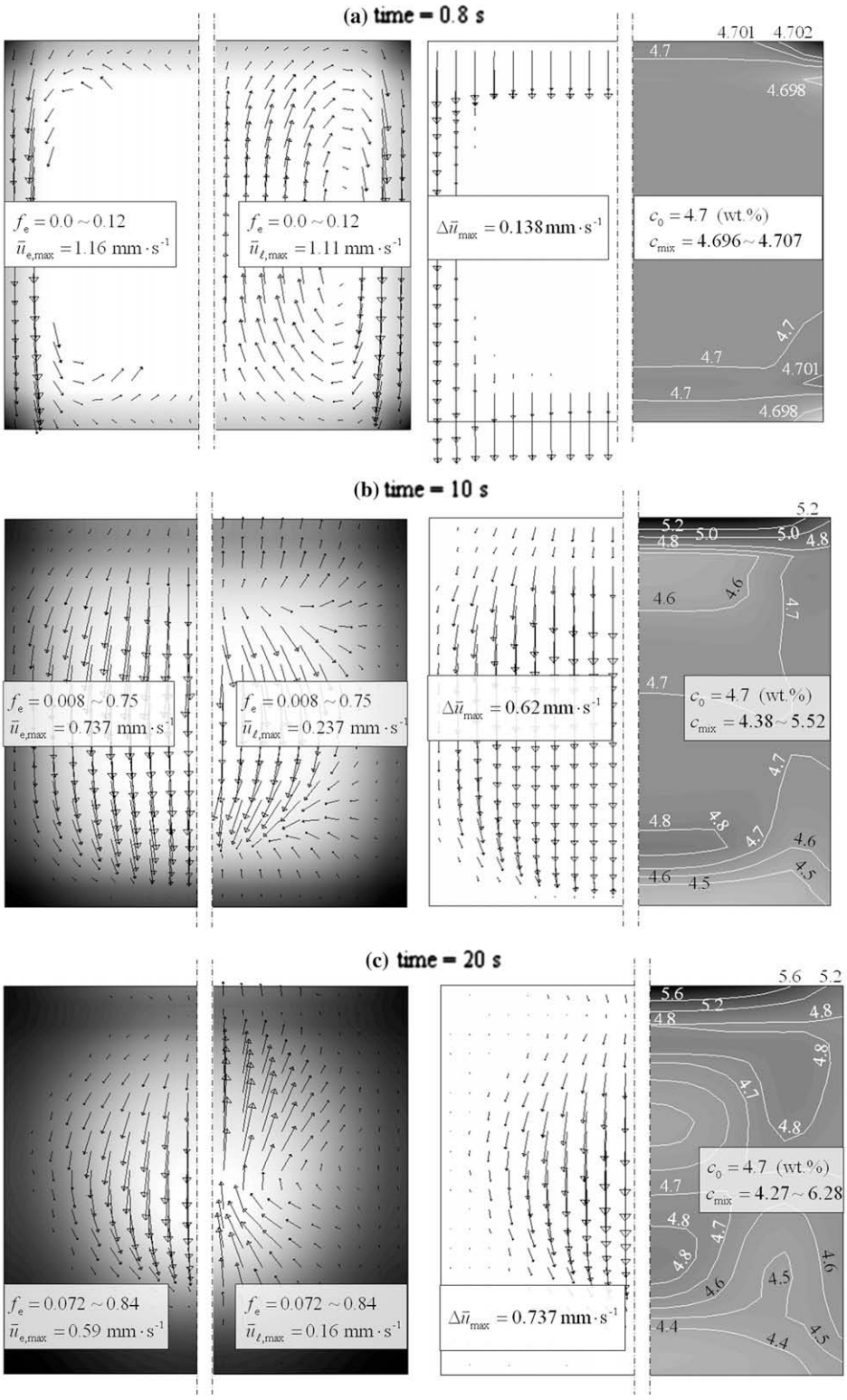


Fig. 9. Solidification sequence of the square casting (Al–4.7 wt.% Cu) predicted with the "pure" globular solidification model [8,9]. The volume fraction of the equiaxed grains $f_e$ is shown using gray scale, with dark for the highest and light for the lowest value. The vectors of velocity fields $\vec{u}_e$ and $\vec{u}_l$ are overlaid with $f_e$. The relative velocity is described by the vector ($\Delta\vec{u} = \vec{u}_e - \vec{u}_l$). The mixture concentration $c_{mix}$ is shown with both gray scale and isolines. Nucleation parameters are: $n_{max} = 5 \times 10^{11}\ m^{-3}$, $\Delta T_\sigma = 2\ K$, $\Delta T_N = 5\ K$.

cation. One reason for this is that less $f_e$ forms according to the globular solidification model at this moment; a second reason is that the relative velocity between the extradendritic melt and the grains, $\Delta\vec{u}$, is smaller. At 10 s, equiaxed grains spread throughout the whole casting. The grains in the region with $f_e$ less than the packing limit continue to

sink downwards. In the upper section, the melt flows upwards and causes the positive segregation near the top surface to become increasingly wide, resulting in stronger positive segregation. The sedimentation process and the induced segregation in the lower section become increasingly pronounced. If compared with the dendritic solidification at the same instant, the macrosegregation is much stronger under globular solidification conditions. This can be explained by the higher solute transfer rate at the grain boundary (envelope) for the globular solidification. The solute transfer rate at the grain boundary between a globular grain and the melt is much stronger than the solute transfer rate at the grain envelope between an interdendritic melt and the extradendritic melt.

As solidification continues (20 s), only the grains in the center of the casting can move. The grains located there continue to sink, while the melt rises. This type of relative motion strengthens the macrosegregation. As previously mentioned, the negative segregation zone in the upper part of the casting is not stable, and it moves with the sinking grains. When it meets the solute-enriched melt coming from below, the negative segregation can be cancelled out, or even reversed to a positive segregation. Similarly, in the lower section of the casting, the "unstable" positive segregation zone is also partially compensated for by the settling grains coming from the upper section.

## 6. Discussion

### 6.1. The numerical model

It is demonstrated that the phenomena accompanying equiaxed dendritic solidification, which were considered in previous models [4,5], can be reproduced using the current model. This includes: the evolution of different phase regions; the competition between the growth of the grain envelope and the solidification of the interdendritic melt; the recalescence phenomenon and its dependence on the nucleation parameters and cooling rates; and the formation of extra- and interdendritic eutectic phases.

It is important to consider the GDT during equiaxed solidification, because the equiaxed grain usually starts to grow with a globular morphology, followed by a dendritic morphology once the GDT occurs. Appolaire and co-workers [10,15,16] suggested a model for the GDT based on the rate of solidification/melting within the grain envelope and the rate of expansion/shrinkage of the envelope. The rate of solidification/melting within the grain was determined according to the mass, energy and species balance; while the rate of expansion/shrinkage of the envelope was deduced based on the dendrite tip growth kinetics. A drawback of this model was that the rate of solidification/melting within the grain was determined based on an assumption of the complete mixing of the interdendritic melt ($c_d = c_\ell^* = \bar{c}_{env}$). The assumption of the complete mixing of the interdendritic melt is not valid at the initial stage (Fig. 3b) according to the current study. Therefore, in the current model, a different approach to simulating the GDT by making a direct comparison of two growth velocities, $v_{glob}$ and $v_{env}$, was proposed. Here $v_{glob}$ was calculated by the diffusion-governed (Zener-type) growth model [8,9], while $v_{env}$ was calculated based on the dendrite tip growth kinetics. As shown in the modeling results (Fig. 3a), the globular growth governs the initial stage, i.e., $v_{glob}$ was larger than $v_{env}$. It was verified that the grains start to grow with globular morphology at the initial stage. Once $v_{env}$ surpasses $v_{glob}$, GDT occurs and "free" dendritic growth commences. The current GDT model has not been verified with classical interface instability theory [13], hence further verification efforts or improvements are necessary.

The evolution of an equiaxed grain can be divided into four stages: initial globular growth (I), free dendritic growth (II), dendritic growth with recalescence (III), and confined dendritic growth or coarsening/dendrite arm thickening (IV).

Comparisons with the experimental results published by Nielsen et al. [10] were made. The total eutectic $f_{Eu}^{total}$ could be quantitatively predicted, as shown in Fig. 7a, especially for the lower composition alloys. The current parameter studies showed that the total eutectic $f_{Eu}^{total}$ is linearly proportional to the alloy composition, and it was not dependent on the grain morphology. The relatively large discrepancy between experimental and modeled $f_{Eu}^{total}$ for the high composition alloys was primarily due to the neglect of the latent heat released during the eutectic reaction and the neglect of back diffusion in the solid phase.

By choosing the proper dendritic morphological parameters, the volume fraction of the extradendritic eutectic phase $f_{Eu}^{extra}$ and the interdendritic eutectic phase $f_{Eu}^{intern}$ could also be quantitatively predicted. However, the simulation results (Fig. 7b and c) show that the extradendritic eutectic $f_{Eu}^{extra}$ and the interdendritic eutectic $f_{Eu}^{intern}$ are strongly dependent on the morphological parameters ($\Phi_{env}$, $\Phi_{sph}$, $\lambda_2$). This suggests that, in future, more attention should be paid to the assumptions and parameters of the grain morphology. One of the major differences in the current model from the previous models is the introduction of two additional grain morphological parameters, $\Phi_{env}$ and $\Phi_{sph}$. The uncertainty regarding these parameters may lead to additional complications with respect to the application of the model, but the parameter studies (Fig. 7) have shown their importance in acquiring accurate quantitative modeling results. Therefore, further modeling or experimental studies to observe the evolution of the grain morphology and to determine quantitatively these morphological parameters are suggested, e.g., the experimental work of Badillo and co-workers [17,18].

Another improvement over previous models was the treatment of the interdendritic melt and its solidification. Complete mixing ($c_\ell^* = c_d = \bar{c}_{env}$) of the interdendritic melt was previously assumed, but in the current model a non-uniform solute distribution in the interdendritic melt region ($c_\ell^* \neq c_d \neq \bar{c}_{env}$), as suggested by WB [4], was considered. The modeling result demonstrated in Fig. 3 shows that $c_d$

could be significantly different from $c_\ell^*$ during the free dendritic growth stage (II) and the recalescence stage (III). The assumption of the complete mixing ($c_d = c_\ell^*$) means that any cause for fluctuation in the local temperature $T$, e.g., due to the convection and grain transport or due to a change in the local cooling condition, would correspondingly impose an immediate change in $c_\ell^*$ (i.e., $c_d$). The change in $c_d$ could only be fulfilled through interdendritic melt solidification/melting. The quantity $c_d$ is "rigidly" coupled with the interdendritic solidification/melting ($M_{ds}$) and hence with the latent heat. This "rigid" coupling among $T$, $c_\ell^*$, $c_d$ and $M_{ds}$ could result in difficulties in obtaining the convergent numerical solution. The major concern regarding the complete mixing assumption was that it could lead to incorrect (inaccurate) results. As reported by RT [5], the cooling curve calculated using the complete mixing assumption was difficult to fit to the experimental results, especially for coarse-grained alloys; for example, the depth of the recalescence was underestimated. Furthermore, according to the current model, the deviation of $\bar{c}_{env}$ from $c_d$ increases at stage II. This deviation decreases progressively during stage III. At the moment of transition from stage II to stage III, the difference between $\bar{c}_{env}$ and $c_d$ reaches its maximum. Obviously, the previous assumption of $\bar{c}_{env}$ equal to $c_d$ would cause an erroneous estimation of the species transfer from the interdendritic melt to the extradendritic melt. This is critical for the calculation of the enrichment of the solute in the extradendritic melt and the final macrosegregation. However, after stage III, the difference between $\bar{c}_{env}$ and $c_d$ becomes very small, and they gradually approach the thermodynamic equilibrium concentration $c_\ell^*$. This indicates that the complete mixing assumption can be valid at the last stage of solidification.

A diffusion-governed solidification model for the interdendritic melt was newly implemented. The driving force for the diffusion was $c_\ell^* - c_d$, and the diffusion length scale was in the order of $\lambda_2$. Note that constant $\lambda_2$ was considered, although $\lambda_2$ may vary with time. However, the parameter studies have shown that the exact value for $\lambda_2$ is of minor importance. The model suggested by WB [4] was employed to calculate the diffusion length and the specific surface area of the d–s interface, but it was modified by accounting for an impingement factor. This simple approach is empirical. However, the inaccuracy caused by this simplicity seems not significant. As expressed in Eqs. (18) and (33)–(35) in Part I, a dominant parameter influencing the solidification rate is the secondary dendrite arm space $\lambda_2$, which determines both the interdendritic diffusion length and the specific surface area of the d–s interface. The solidification rate $M_{ds}$ is proportional to $(1/\lambda_2)^2$. The current paper varies $\lambda_2$ from 10 to 40 μm, corresponding to a reduction in $M_{ds}$ by a factor of 1/16. The modeling results (Fig. 7), however, show that the predicted $f_{Eu}^{total}$, $f_{Eu}^{extra}$ and $f_{Eu}^{intern}$ are insensitive to this variation. This implies that the space to improve the model for the solidification of the interdendritic melt ($M_{ds}$) is quite limited.

The method of treating the interdendritic melt flow and grain movement proposed by WB [1] was simplified in the current model. In the WB model [1], the interdendritic melt and the extradendritic melt were treated as one mixture phase, for which a set of momentum equations were solved. A concept of the flow partitioning between the interdendritic melt and extradendritic melt was introduced through a partitioning tensor. The slow flow of the interdendritic melt in relation to the solid dendrites could also be considered. This slow interdendritic melt flow could be important in the high grain volume fraction region when the grains are impinged upon one another and the volume fraction of the extradendritic melt approaches zero. In the current model, the interdendritic melt is considered part of the grain. The interdendritic melt shares the same velocity with the solid dendrites, but it is separated from the extradendritic melt. The interdendritic melt behaves as part of a grain rather than as part of an extradendritic melt. Consequently, no supplementary correlation was needed to determine the flow partitioning tensor. Nevertheless, reasonable results were obtained. The current model predicts that the intensity of the macrosegregation in a $40 \times 40\ mm^2$ Al–4.7 wt.% Cu casting falls by $c_0 \pm 0.068 \times c_0$. With regard to laboratory conditions, for example, a cylindrical casting (Al–1 wt.% Cu and Al–10 wt.% Cu) with diameter 18 mm and height 100 mm height under a cooling rate of ~12–24 K $s^{-1}$ shows the maximum positive and negative segregation in the range $c_0 \pm 0.2 \times c_0$ [11].

### 6.2. The equiaxed solidification

The calculated $f_s$–$T$ curve was found to superimpose the Scheil curve during the last stages of solidification (Fig. 4), but a significant discrepancy was found early in the free dendrite growth and recalescence stages. This finding agrees with that of RT [5]. The predicted eutectic $f_{Eu}^{total}$ also agreed with the result estimated by Scheil model. The total eutectic phase formed was slightly influenced by the cooling rate, but this is strongly dependent on the alloy composition. The volume fraction of the eutectic is linearly proportional to the alloy composition (Fig. 7). This conclusion is supported by the experimental results [10].

The dependence of $f_{Eu}^{total}$ on the cooling rate was also investigated. The cooling rates at different locations across the square casting section are different. Although the corner has a higher cooling rate, there is only marginally less $f_{Eu}^{total}$ than in the center of the casting. For example, an Al–4.7 wt.% Cu casting simulation shows 10.3 wt.% of eutectic at the corner, and 10.5 wt.% in the center. The lower cooling rate tends to favor the eutectic formation. Many experimental results with respect to this issue are contradictory, but a general opinion tends to support the above finding. Provided the cooling rate is sufficiently large (e.g., >1 K $s^{-1}$) that the back diffusion in solid dendrites can be neglected, the lower cooling rates favor the eutectic formation [12]. The current model ignored back diffusion in the solid.

Distinguishing the interdendritic eutectic from the extradendritic eutectic, larger cooling rates favor the formation of the interdendritic eutectic phase, while lower cooling rates favor the extradendritic eutectic. An obvious reason for this is that low cooling rates allow around-grain diffusion more efficiently, i.e., more of the solute element is diffused into the extradendritic melt, forming more extradendritic eutectic at the end of solidification.

The influence of grain sedimentation on macrosegregation was evident. Two main mechanisms operate under these conditions: one mechanism is the replacement of the solute-rich melt by solute-depleted grains, which induces a negative segregation; the second mechanism is the replacement of the solute-depleted grains by the solute-rich melt, which induces a positive segregation. Other macrosegregation formation mechanisms during equiaxed solidification were studied elsewhere [19,20].

## 7. Conclusions

The modified equiaxed solidification model was successfully verified to be able to simulate the complete equiaxed solidification process. This includes a series of accompanying phenomena such as nucleation, the start of globular growth, the GDT, dendritic growth and evolution of different phase regions, recalescence, the formation of the final microstructure (grain size, inter- and extradendritic eutectic distributions) and macrosegregation. Almost all the features of previous models with respect to globular and dendritic solidification were considered by the current model. Further new features were also explored: the GDT; two morphological parameters ($\Phi_{env}$ and $\Phi_{sph}$) were proposed to simplify the equiaxed dendritic grain morphology; a non-uniform solute distribution in the interdendritic melt region; and a simplified WB model [1] to handle the two-phase flow. Comparisons with published experimental results [10] were made, and quantitative agreement with respect to the formation of the interdendritic and extradendritic eutectic phase was obtained. Nevertheless, further experimental verification is still desired. The parameter studies showed the importance of some model assumptions/parameters: (1) the assumption of the dendritic grain morphology and its parameters, $\Phi_{env}$ and $\Phi_{sph}$; (2) the determination of the diffusion lengths of the interdendritic and extradendritic melts. Uncertainty of the above parameters would influence the quantitative accuracy of the modeling results.

The illustrative modeling results from an Al–Cu binary alloy casting provided a better understanding of equiaxed dendritic solidification.

1. The local volume fraction of the total eutectic phase $f_{Eu}^{total}$ is linearly proportional to the alloy composition, and independent of the assumed grain morphology (e.g., $\Phi_{env}$, $\Phi_{sph}$).
2. The cooling rate has a very minor influence on total eutectic $f_{Eu}^{total}$. As diffusion in the solid phase is ignorable, the lower cooling rate marginally favors total eutectic formation.
3. The influence of cooling rate on the interdendritic eutectic $f_{Eu}^{intern}$ and extradendritic eutectic $f_{Eu}^{extra}$ is evident. A large cooling rate favors the formation of $f_{Eu}^{intern}$, while a lower cooling rate favors the formation of $f_{Eu}^{extra}$ .
4. The grain sedimentation and the sedimentation-induced melt convection play a dominant role in the formation of macrosegregation during equiaxed solidification. There are two main mechanisms: one is the replacement of the solute-rich melt by solute-depleted grains, which induces negative segregation; the second is the replacement of the solute-depleted grains by solute-rich melt, which induces positive segregation.
5. "Pure" globular equiaxed solidification tends to exhibit more macrosegregation than dendritic solidification.

## References

[1] Wang CY, Beckermann C. Metall Mater Trans 1996;27A:2754.
[2] Wang CY, Beckermann C. Metall Mater Trans 1996;27A:2765.
[3] Beckermann C, Wang CY. Metall Mater Trans 1996;27A:2784.
[4] Wang CY, Beckermann C. Metall Trans 1993;24A:2787.
[5] Rappaz M, Thévoz Ph. Acta Metall 1987;35:1478.
[6] Rappaz M, Thévoz Ph. Acta Metall 1987;35:2929.
[7] Rappaz M, Boettinger WJ. Acta Mater 1999;47:3205.
[8] Ludwig A, Wu M. Metall Mater Trans 2002;33A:3673.
[9] Wu M, Ludwig A, Bührig-Polaczek A, Fehlbier M, Sahm PR. Int J Heat Mass Transfer 2003;46:2819.
[10] Nielsen Ø, Appolaire B, Combeau H, Mo A. Metall Mater Trans 2001;32A:2049.
[11] Rerko RS, Groh HC, Beckermann C. Mater Sci Eng A 2003;347:186.
[12] Eskin D, Du Q, Ruvalcaba D, Katgermann L. Mater Sci Eng A 2005;405:1.
[13] Kurz W, Fisher DJ. Fundamentals of solidification. 4th ed. Switzerland: Trans. Tech. Publication; 1998.
[14] Lipton J, Glicksman ME, Kurz W. Mater Sci Eng 1984;65:57.
[15] Appolaire B. Ph.D. Thesis, Institut National Polytechnique de Lorraine, France; 1999.
[16] Appolaire B, Combeau H, Lesoult G. Mater Sci Eng A 2008;487:33.
[17] Badillo A, Ceynar D, Beckermann C. J Cryst Growth 2007;309:197–215.
[18] Badillo A, Ceynar D, Beckermann C. J Cryst Growth 2007;309:216–24.
[19] Wu M, Ludwig A, Luo J. Mater Sci Forum 2005;475–479(1–5):2725.
[20] Wu M, Könözsy L, Ludwig A, Schützenhöfer W, Tanzer R. Steel Res Int 2008;79(8):637.